Enhanced Intrinsic Excitability in Basket Cells Maintains Excitatory-Inhibitory Balance in Hippocampal Circuits

Emilie Campanac, Célia Gasselin, Agnès Baude, Sylvain Rama, Norbert Ankri, Dominique Debanne

HAL Id: hal-01774392

https://amu.hal.science/hal-01774392

Submitted on 23 Apr 2018

Enhanced Intrinsic Excitability in Basket Cells Maintains Excitatory-Inhibitory Balance in Hippocampal Circuits

Emilie Campanac[1,2,5], Célia Gasselin[1,2,5], Agnès Baude[2,3,4], Sylvain Rama[1,2], Norbert Ankri[1,2] and Dominique Debanne[1,2] *

[1]INSERM, UMR_S 1072, F-13344 Marseille, France
[2]Aix-Marseille Université, UNIS, F-13344 Marseille, France
[3]CNRS, UMR6231, F-13344 Marseille, France
[4]INSERM, INMED, U901, F-13273 Marseille, France
[5]These authors equally contributed to this work

Highlights

The dynamics of inhibitory circuits is thought to rely on synaptic modifications

Results show that basket cells express persistent increase in neuronal excitability

This plasticity depends on mGluR5 and involves the regulation of Kv1 channels

This plasticity facilitates recruitment of basket cells to balance excitation

SUMMARY

The dynamics of inhibitory circuits in the cortex is thought to rely mainly on synaptic modifications. We challenge this view by showing that hippocampal parvalbumin-positive basket cells (PV-BCs) of the CA1 region express long-term (>30 min) potentiation of intrinsic neuronal excitability (LTP-IEPV-BC) upon brief repetitive stimulation of the Schaffer collaterals. LTP-IEPV-BC is induced by synaptic activation of metabotropic glutamate receptor subtype 5 (mGluR5) and mediated by the downregulation of Kv1 channel activity. LTP-IEPV-BC promotes spiking activity at the gamma frequency (~35 Hz) and facilitates recruitment of PV-BCs to balance synaptic and intrinsic excitation in pyramidal neurons. In conclusion, activity-dependent modulation of intrinsic neuronal excitability in PV-BCs maintains excitatory-inhibitory balance and thus plays a major role in the dynamics of hippocampal circuits.

INTRODUCTION

Excitation and inhibition walk hand in hand in cortical circuits (Isaacson and Scanziani, 2011). This excitatory-inhibitory balance is thought to maintain activity within physiological bounds and shape cortical activity in space and time. Excitatory-inhibitory balance can be transiently perturbed by learning but generally recovers after a few tens of minutes (Froemke et al., 2007). Classically, activity-dependent plasticity of inhibitory circuits is thought to be achieved by the persistent enhancement of excitatory synaptic drive to inhibitory interneurons (Alle et al., 2001; Kullmann and Lamsa, 2007; Kullmann et al., 2012; Lamsa et al., 2007; Maccaferri et al., 1998; Pelletier and Lacaille, 2008). For instance, feed-forward and feedback interneurons in the CA1 region of the hippocampus both express long-term synaptic potentiation (Lamsa et al., 2005; Lamsa et al., 2007). However, functional plasticity might also be achieved through the regulation of voltage-gated ion channels that control synaptic integration and spike initiation (Debanne and Poo, 2010; Zhang and Linden, 2003). Persistent activity-dependent plasticity of intrinsic neuronal excitability has been reported in CA1 hippocampal principal cells (Campanac et al., 2008; Campanac and Debanne, 2008; Daoudal et al., 2002; Wang et al., 2003) but whether GABAergic interneurons express use-dependent intrinsic plasticity has yet to be addressed (Miles and Poncer, 1993; Miller et al., 2011; Ross and Soltesz, 2001; Sun, 2009; Yazaki-Sugiyama et al., 2009).

We show here that in area CA1 feed-forward inhibition is mostly enhanced by high-frequency stimulation of the Schaffer collaterals through a persistent increase in intrinsic neuronal excitability in a subset of GABAergic interneurons of the CA1 region. This intrinsic plasticity requires synaptic stimulation of metabotropic glutamate receptor type 5 and is mediated by the downregulation of voltage-gated potassium channels.

RESULTS

Enhanced Feed-Forward Inhibition in Area CA1: Contribution of PV-BCs

We recorded from CA1 pyramidal neurons in hippocampal slice (see Experimental Procedures). Compound excitatory and inhibitory postsynaptic potentials were evoked by stimulation of the Schaffer collaterals (Figure 1A; see Figure S1 available online). High-frequency stimulation (HFS) of the Schaffer collaterals (10 trains of 10 pulses at 100 Hz, delivered at a frequency of 0.3 Hz) resulted not only in potentiation of synaptic excitation, but also increased disynaptic inhibition in CA1 pyramidal neurons (Figure 1A). Monosynaptic excitatory postsynaptic potentials (EPSPs) onto interneurons that are initially subthreshold may cross the spike threshold after HFS. In order to test this hypothesis, fast-spiking interneurons were recorded in whole-cell configuration in the stratum pyramidale of the CA1 region (see Experimental Procedures). Their resting membrane potential was −67.6 ± 0.7 mV (n = 12). The great majority of these cells were parvalbumin-positive (10/12; Figure 1B). Their axonal arborization, labeled with biocytin, was confined within the pyramidal cell layer (9/9; Figure 1B), indicating that they were putative parvalbumin-positive basket cells (PV-BCs; (Freund and Katona, 2007; Glickfeld and Scanziani, 2006; Gulyás et al., 2010; Szabó et al., 2010)). PV-BCs typically fired action potentials (APs) in clusters and the first spike, upon a slow depolarizing ramp, occurred generally with a delay (Goldberg et al., 2008).

We first examined whether recruitment of PV-BCs was altered after HFS. Initially, the probability of evoking an AP by the synaptic input was very low (0.07 ± 0.06, n = 5), indicating that they were not recruited by excitatory inputs before HFS. In contrast, the firing probability markedly increased 15–30 min after HFS (to 0.50 ± 0.15, n = 5; Wilcoxon, p < 0.07; Figure 1C), showing that PV-BCs were

recruited by the stimulated synaptic pathway. We next examined whether the origin of this increased firing was synaptic or intrinsic. Excitatory synaptic transmission was found to be enhanced after HFS (155% ± 7% of the control EPSP slope, n = 5; Figure 1D), suggesting that the observed facilitation in spiking activity may partly result from facilitation in synaptic excitation. To determine whether intrinsic excitability was enhanced in PV-BCs, synaptic circuits were bypassed by directly simulating families of near-threshold EPSPs in PV-BC with the dynamic-clamp technique (Figure 1E). The input-output function of PV-BCs was found to be strengthened 15–30 min after HFS (Figure 1E). These data indicate that intrinsic neuronal excitability of PV-BC is persistently enhanced, independently of any modification in excitatory synaptic circuits. Next, we estimated the respective contributions of synaptic and intrinsic changes in the recruitment of PV-BC after HFS. Synaptic and intrinsic changes were estimated from the EPSP-spike curves established before and 10–30 min after HFS. The firing probability was measured on the control and post-HFS curves for the initial value of EPSP-slope (3.4 mV/ms; gray arrow in Figure 1F) and for that obtained after HFS (5.4 mV/ms; red arrow in Figure 1F). The data indicate that a large proportion (~80%) of the increased firing probability results from an increase in intrinsic excitability.

LTP-IE in PV-BC Is Mediated by mGluR5

In order to fully characterize the induction and expression mechanisms of this novel form of intrinsic plasticity in PV-BCs, moderate spiking activity (8–10 spikes) was triggered with pulses of depolarizing current (800 ms). To verify that the HFS-induced increase in intrinsic neuronal excitability did not result from a change in background GABAergic inhibition, experiments were performed in the presence of the GABAA channel blocker, picrotoxin (100 μM). After recording a stable baseline, high frequency stimulation (HFS) was delivered to the synaptic pathway. HFS produced a transient increase in spike number (247% ± 29% of the control, n = 9, measured at +1 min) followed by a stable plateau of enhanced excitability (209% ± 41% of the control spike number, n = 9, measured at 25–30 min; Figure 2A). While the short-term increase in excitability was associated with a transient depolarization of the membrane potential by ~2–3 mV (104% ± 1% of the control membrane potential measured at +2 min), the long-term component (LTP-IE$_{PV-BC}$) measured at 25–30 min was totally independent of any change in membrane potential (100.1% ± 0.5%, n = 9) or input resistance (99% ± 2%, n = 9). Other subthreshold parameters such as the membrane time constant (τm = 20.1 ± 2.4 ms before HFS and 20.4 ± 2.1 ms after, Wilcoxon p > 0.5; Figure S2) or the resonance properties (Figure S2) remained unchanged after induction of LTP-IE$_{PV-BC}$. Firing accommodation was not altered after induction of LTP-IE$_{PV-BC}$ (first ISI / last ISI: 1.44 ± 0.27 before and 1.19 ± 0.11 after HFS; Wilcoxon p > 0.5). No change in excitability was observed in the absence of HFS (107% ± 1%, n = 7; Wilcoxon p > 0.05; Figure S2).

Long-term synaptic modifications in hippocampal interneurons require a wide range of glutamate receptors including ionotropic and metabotropic glutamate receptors (Kullmann and Lamsa, 2007; Pelletier and Lacaille, 2008). To test whether AMPA or NMDA receptors are required for LTP-IE$_{PV-BC}$ induction, HFS was delivered in the presence of 2 mM kynurenate. Although the transient component was diminished (137% ± 7% of the control, n = 9, measured at +1 min), no significant reduction in LTP-IE$_{PV-BC}$ was observed (211% ± 20%, n = 11, measured at 25–30 min, Mann-Whitney U test, p > 0.2); Figure 2B), indicating that NMDA and AMPA receptor activation does not play a critical role in LTP-IE$_{PV-BC}$. Next, the role of metabotropic glutamate receptor (mGluR) activation was tested. HFS failed to induce LTP-IE$_{PV-BC}$ in the presence of 2 mM kynurenate and 10 μM of the mGluR type 5-selective antagonist, MPEP (97% ± 11%, n = 9) or in the presence of MPEP alone (10 μM; 111% ± 7% n = 5; Mann-Whitney U test, p < 0.05; Figure 2C). LTP-IE$_{PV-BC}$ was also observed following brief

application of the mGluR1/5 agonist, DHPG (20 µM; 169% ± 42%, n = 5) or the mGluR5 agonist CHPG (200–500 µM; 297% ± 72%, n = 9; Figure 3A). To verify that other neurotransmitter/neuromodulators were not necessary to the induction of LTP-IE$_{PV-BC}$, experiments were performed in the presence of the broad spectrum calcium channel blocker cadmium. Cadmium (50 µM) totally abolished evoked synaptic responses. In the presence of cadmium, CHPG (500 µM) still induced an increase in excitability that was similar to that induced in control saline (199% ± 45%, n = 7, Mann-Whitney U test, p > 0.5; Figure 3B). Thus, although AMPA/NMDA receptors are involved in the short-term increase in excitability in PV-BCs, activation of mGluR5 is necessary and sufficient for the induction of LTP-IE$_{PV-BC}$.

Mechanisms of LTP-IE in PV-BCs: Role of Kv1 Channels

We next investigated the expression mechanisms of LTP-IEPV-BC. Fast spiking PV-BCs display delayed firing, which is a typical hallmark of the slowly inactivating D-type K+ current mediated by Kv1 channels (Cudmore et al., 2010; Goldberg et al., 2008; Li et al., 2012). A striking feature of LTP-IEPV-BC induced by HFS or application of mGluR agonist is the marked reduction (∼50%) in the latency of the first spike (Figures 4A and 4B). The temporal change in firing was analyzed on spike histograms. In fact, both phasic (100–300 ms) and tonic spiking activity increased (Figure 4C).

The reduced delay in the first spike latency suggests that the D-type potassium current (I_D) carried by Kv1 channel is downregulated following LTP-IEPV-BC induction. In fact, PV-positive interneurons in the stratum pyramidale were found to express high levels of Kv1.1 (Figure 5A) and Kv1.2 (Figure S3) channels in both the cell body and their axon initial segment (AIS). Blocking Kv1 channels with 4-AP (5–10 µM) or DTx-I (100–150 nM) reduced the first spike latency (21% ± 11% of the control, n = 15) and strongly increased spiking activity (402% ± 45% of the control spike number, n = 15; Figure 5B), thus mimicking LTP-IE$_{PV-BC}$.

The reduced delay in the first spike suggests that the D-type potassium current (I_D) carried by Kv1 channel is downregulated following LTP-IE$_{PV-BC}$ induction. If this hypothesis is correct, LTP-IE$_{PV-BC}$ should be occluded by the pharmacological inactivation of I_D. In fact, in the presence of 100–150 nM DTx-I or 5–10 µM 4-AP, HFS failed to induce LTP-IE$_{PV-BC}$ (102% ± 8%, n = 7, and 106% ± 4%, n = 5, respectively; Figures 5C and S3). In these experiments, the amplitude of the current step was adjusted to elicit a non-saturating number of spikes in control conditions (8–10 spikes/s; Figures 5C and S3). Furthermore, the delay to the first spike remained unchanged in the presence of Kv1 channel blockers (4-AP: 89% ± 8%, n = 5, and DTx-I: 126% ± 22%, n = 7; Figure S3), indicating that all features of LTP-IE$_{PV-BC}$ are suppressed when Kv1 channels are blocked.

We next examined the cellular mechanism of mGluR5-dependent regulation of Kv1. The translation of Kv1.1 channel mRNA and surface expression of Kv1.1 channels is strongly inhibited by the mammalian target of rapamycin mTOR (Raab-Graham et al., 2006). mTOR is also activated by mGluR5 through the PI3K/Akt pathway (Klann and Dever, 2004). We therefore tested whether LTP-IE$_{PV-BC}$ was affected by the inhibition of mTOR with rapamycin. LTP-IE$_{PV-BC}$ was significantly reduced in PV-BCs treated for 2 hr with rapamycin (50 nM; 122% ± 20%, n = 5, versus 212% ± 29%, n = 8, Wilcoxon, p < 0.07; Figure 5D). We conclude that LTP-IE$_{PV-BC}$ is expressed through an mGluR5-dependent downregulation of Kv1 channel activity involving mTOR.

Hyperpolarization of the Spike Threshold after LTP-IEPV-BC

Kv1 channels are generally localized at the AIS where they control the spike threshold (Goldberg et al., 2008; Higgs and Spain, 2011; Nusser, 2009). We therefore examined whether changes in spike threshold occurred following induction of LTP-IE$_{PV-BC}$. As reported earlier, the voltage threshold of the first AP was relatively depolarized (-35.7 ± 1.1 mV, n = 9). It is noteworthy that the spike threshold was found to be hyperpolarized by 3.9 ± 1.1 mV (n = 9), 15–30 min after HFS (Figure 6A). These data indicate that the global responsiveness of PV-BCs is enhanced following HFS and that subthreshold EPSPs might be able to elicit an action potential after induction of LTP-IE$_{PV-BC}$. The HFS-induced hyperpolarization of the spike threshold was perfectly mimicked by pharmacological inactivation of Kv1 channels with DTx-I. The voltage threshold of the first AP was hyperpolarized by 11.1 ± 1.1 mV (n = 9) in the presence of DTx-I (Figure 6B). Similar changes in firing profile were obtained in a model of PV-BC upon blockade of Kv1 channels at the axon or the cell body (Figure S4), suggesting that regulation of axonal or somatic Kv1 channels may equally account for LTP-IEPV-BC (Golomb et al., 2007). However, change in spike threshold reached the level observed experimentally only if Kv1 channels were suppressed in the axon. In order to further confirm that PV-BC recruitment was enhanced by the Kv1-dependent hyperpolarization of the spike threshold, we examined the effect of the pharmacological blockade of Kv1 on disynaptic inhibition. As expected, DTx-I mimicked the effect of HFS by increasing disynaptic inhibition in CA1 pyramidal neurons (Figure 6C). Interestingly, the enhanced disynaptic inhibition induced by HFS or by CHPG was importantly reduced or occluded by DTx-I (HFS; 186% $\pm$ 13%, n = 6, versus 323% $\pm$ 19%, n = 7, in control; CHPG: 96% $\pm$ 8%, n = 7, versus 147% $\pm$ 8%, n = 7, in control; Figure 6D). Thus, these data confirm that the facilitation of feed-forward inhibition is predominantly mediated by the regulation of intrinsic excitability. We conclude that mGluR5 and Kv1-dependent LTP-IE$_{PV-BC}$ promote disynaptic inhibition in CA1 circuits.

LTP-IEPV-BC Promotes Spiking Activity in the γ Frequency Range

Fast-spiking PV-BCs display a specific mode of firing composed of sparse and clustered APs (Goldberg et al., 2008). Sparse spikes (Sps) typically occurred in our recordings after a slow depolarizing ramp of potential at an instantaneous frequency of $\sim$10 Hz (Figures 7A and S5S5). In contrast, clustered spikes (Cls) followed immediately an AP and displayed a much more hyperpolarized voltage threshold. Consequently, their instantaneous frequency was much higher and corresponded to the gamma (γ)-frequency range (25–50 Hz). We therefore examined whether Sps and Cls were equally altered following induction of LTP-IE$_{PV-BC}$. Surprisingly, the enhanced excitability was mostly supported by an increase in the proportion of Cls (from 69% $\pm$ 9% to 92% $\pm$ 3%; Figure 7A). In fact, a clear gain of spiking activity in the γ frequency range was observed after HFS (Figure 7B). In order to check that the observed changes were not dependent on the type of depolarizing profile, trains of simulated EPSPs were injected in PV-BCs. A similar increase in the γ range was observed after HFS (Figure S5). Thus, mGluR5 stimulation increases intrinsic neuronal excitability of PV-BC and promotes their firing in the γ range.

Regular Spiking PV-Negative Interneurons Do Not Express LTP-IE

We next determined whether HFS-induced increase in intrinsic excitability was specific to PV-BCs. A second class of interneuron was recorded in the stratum pyramidale of the CA1 region. In contrast to PV-BCs, these interneurons fired regularly (CV of the fifth interspike interval 0.04 $\pm$ 0.01, n = 25 versus 0.67 $\pm$ 0.10, n = 27 for PV-BCs; Figure 8A), displayed a high input resistance (476 $\pm$ 48 MΩ, n =

20 versus 120 ± 9 MΩ n = 22 for PV-BCs, Mann-Whitney U test p < 0.01) and had a low rheobase (56 ± 5 pA, n = 20 versus 204 ± 13 pA, n = 22 for PV-BCs, Mann-Whitney U test, p < 0.01). None of regular spiking (RS) neurons expressed PV (0/13; Figure 8B). Most importantly, HFS failed to induce LTP-IE in these interneurons (91% ± 4%, n = 7; Figure 8C). Furthermore, bath application of the type I mGluR agonist, DHPG (20 μM) or the specific mGluR5 agonist CHPG (200–500 μM) induced no increase in intrinsic excitability (91% ± 11%, n = 7, and 80% ± 7%, n = 7; Figure S6). Taken together, these results indicate that LTP-IE is specifically expressed in CA1 PV-BCs.

DISCUSSION

We report here an unexpected form of intrinsic plasticity in PV-BCs of the CA1 region. In addition to the short-term increase in excitability reported earlier (Miles and Poncer, 1993), HFS also induced a persistent increase in intrinsic neuronal excitability (LTP-IE$_{PV-BC}$). LTP-IE$_{PV-BC}$ has two major functional consequences. Together with synaptic modification, LTP-IE$_{PV-BC}$ facilitates feed-forward inhibition in CA1 circuits. In addition, it promotes firing in the gamma range. Interestingly, this intrinsic plasticity was absent in another class of parvalbumin-negative interneurons which display regular firing.

Long-Lasting Enhancement of Feed-Forward Inhibition: A Major Contribution of Intrinsic Excitability in PV-BCs

We show here that HFS of the Schaffer collateral induced a persistent increase in feed-forward inhibition in CA1 pyramidal neurons. The enhanced recruitment of inhibition is likely to be achieved by an increase in the intrinsic excitability of PV-BCs. Initially, PV-BCs are almost silent because of their low input resistance (~120 MΩ for constant depolarization, but only ~50 MΩ for oscillatory input at 40 Hz [Figure S2]) and their depolarized spike threshold (−37 mV). Similar values of spike threshold have been reported in PV interneurons (Goldberg et al., 2008). The depolarized spike threshold essentially results from the high level of Kv conductance. Blockade of Kv1 channels with DTx-I hyperpolarizes the spike threshold by 11 mV (Figure 6B).

Although both synaptic and intrinsic changes contribute to the recruitment of GABAergic inhibition, intrinsic changes take a much larger part in this process. First, EPSP-spike curves reveal that the expected increase in spiking activity resulting from pure synaptic changes is limited to ~20% whereas intrinsic changes represent ~80% (Figure 1F). In addition, when Kv1 channels are blocked with DTx-I, the remaining increase in HFS-induced feed-forward inhibition represents only 39% of the control increase, confirming that more than 60% result from modulation of intrinsic excitability. Thus, intrinsic changes represent a powerful means of recruiting PV-BC interneurons in CA1 circuits.

Induction of LTP-IE$_{PV-BC}$: mGluR5

HFS of the Schaffer collaterals induced two types of changes in PV-BCs: a short-term increase followed by a plateau of potentiation. The short-term enhancement is concomitant with a postsynaptic depolarization and is also observed upon application of mGluR agonists. This initial component was markedly reduced in the presence of kynurenate. A possible explanation is that the total amount of glutamate release during HFS is reduced in the presence of kynurenate because polysynaptic circuits are most likely blocked.

Long-lasting increase in excitability, resulting from persistent cell depolarization has been reported in basket cells of the dentate gyrus (Ross and Soltesz, 2001). In contrast, LTP-IE$_{PV-BC}$ in the CA1 region is independent of any depolarization of the recorded neuron. We show that LTP-IEPV-BC is mediated by an mGluR5-dependent reduction in Kv1 channel activity, possibly resulting from the mTOR-dependent disruption of Kv1.1 channel turnover (Raab-Graham et al., 2006). In fact, HFS produced no change in intrinsic excitability in the presence of the specific mGluR5 antagonist MPEP. In addition, LTP-IE$_{PV-BC}$ could be induced either by the brief application of the mGluR1/5 agonist DHPG or the specific mGluR5 agonist CHPG. LTP-IE$_{PV-BC}$ could be also induced by CHPG in the presence of the broad spectrum calcium channel blocker cadmium, indicating that other neurotransmitters/neuromodulators might not play a critical role in the induction of LTP-IE$_{PV-BC}$. Thus, mGluR5 stimulation is necessary and sufficient for the induction of LTP-IE in PV-BCs.

Expression of LTP-IE$_{PV-BC}$: Kv1

Three lines of evidence indicate that expression of LTP-IE$_{PV-BC}$ is mediated by the downregulation of Kv1 channel activity. First, the profile of discharge was considerably altered following induction of LTP-IE$_{PV-BC}$. The delay in the first spike was reduced by ~40%. This effect could be mimicked by Kv1 channel blockers. Second, LTP-IEPV-BC was occluded upon blockade of Kv1 channels with DTx-I or 4-AP. Finally, the hyperpolarization of the spike threshold following LTP-IE could be mimicked by the specific Kv1 channel blocker DTx-I. In PV-BCs, Kv1 channels are principally located in the cell body and the proximal region of the axon. The location of regulated channels has not been precisely determined in this study. However, the large hyperpolarization of the spike threshold after induction of LTP-IE$_{PV-BC}$ argues for a regulation of Kv1 channels in the axon (Goldberg et al., 2008). In fact, a simple model of PV-BCs indicates that regulation of Kv1 channels in the axonal compartment is associated with a large shift in the spike threshold. A major consequence of the axosomatic location of Kv1 is that in contrast to certain forms of intrinsic plasticity reported in the dendrites of CA1 pyramidal neurons (Campanac and Debanne, 2008; Daoudal et al., 2002; Frick et al., 2004), LTP-IEPV-BC is not input specific. Rather LTP-IE$_{PV-BC}$ corresponds to a global increase in excitability (Sourdet et al., 2003; Zhang and Linden, 2003). A direct demonstration of this property is provided by the large change in excitability observed when the neuron is depolarized by current injection in the cell body (Figures 1E and 2A).

Excitatory-Inhibitory Balance

LTP-IE$_{PV-BC}$ contributes to balancing excitation and inhibition when synaptic and intrinsic excitation is enhanced in principal neurons. It therefore constitutes a form of homeostatic plasticity in CA1 microcircuits (Desai, 2003). The overall consequence of the increase in disynaptic inhibition on the ultimate output from pyramidal cells has not been tested here. However, in a previous study, we have shown using the same induction paradigm that, in the presence of inhibition, HFS increased the spiking activity of CA1 pyramidal neurons by +140% (Daoudal et al., 2002). Thus, the increased output from PV-BCs is unlikely to be able to overcome the large potentiation in excitation.

The lack of LTP-IE$_{PV-BC}$ may constitute a privileged target for neurological disorders in which the excitation-inhibition balance is altered (Lewis et al., 2012; Yu et al., 2006). Additional experiments will be required to determine the importance of the regulation of PV-BC excitability in brain diseases.

LTP-IE$_{PV-BC}$ Promotes Spiking Activity in the Gamma Range

A major consequence of LTP-IE$_{PV-BC}$ is the facilitation of spike firing in cluster at the gamma frequency. Previous studies showed that stimulation of excitatory synaptic inputs elicit mGluR-dependent gamma oscillation in the CA1 region (Whittington et al., 1995). Our study extends this view by now showing that the propensity of firing in the gamma range is enhanced in PV-BCs, the main neuronal type orchestrating hippocampal oscillations. Thus, our data suggests use-dependent modulation of hippocampal gamma oscillations.

One may speculate that LTP-IE in PV-BC could have other consequences during slow oscillatory activity. PV-BCs fire with a phase lag during theta activity in vivo (Klausberger and Somogyi, 2008). Our data indicate that the firing lag of PV-BCs is reduced and that the net phasic spiking activity is increased, suggesting that after induction of LTP-IE$_{PV-BC}$ this lag could be diminished. Further investigations will be required to precisely evaluate the contribution of LTP-IE$_{PV-BC}$ to the dynamics of cortical oscillations *in vivo*.

EXPERIMENTAL PROCEDURES

Slice Preparation and Electrophysiology

Hippocampal slices (350–400 µm) were prepared from postnatal day 15–20 Wistar rats. All experiments were carried out according to the European and institutional guidelines for the care and use of laboratory animals (Council Directive 86/609/EEC and French National Research Council). Rats were deeply anesthetized with chloral hydrate (intraperitoneal, 200 mg/kg) and killed by decapitation. Slices were cut with a vibratome (Leica VT-1000S) in a solution containing (in mM: sucrose, 280; NaHCO3, 26; D-glucose, 10; KCl, 1.3; CaCl2, 1; MgCl2, 10). The slices were maintained for one hour at room temperature in oxygenated (95% O2/5% CO2) artificial cerebrospinal fluid (ACSF; in mM: NaCl, 125; KCl, 2.5; NaH2PO4, 0.8; NaHCO3, 26; CaCl2, 3; MgCl2, 2; D-Glucose, 10). Each slice was transferred to a temperature-controlled (29°C) recording chamber with oxygenated ACSF. Neurons were visualized in DIC infrared (IR)-videomicroscopy for patch-clamp experiments. In all recordings from interneurons, GABAA receptors were blocked with picrotoxin (PTx, 100 µM). The area CA1 was surgically isolated to prevent epileptiform bursting. Whole-cell patch-clamp recordings were obtained from CA1 interneurons. The electrodes were filled with an internal solution containing (in mM): K-gluconate, 120; KCl, 20; HEPES, 10; EGTA, 0.5; MgCl26H2O, 2; Na2ATP, 2. Whole-cell recordings from fast-spiking interneurons were obtained with high resistance pipettes (8–10 MΩ) to better preserve integrity of metabotropic signaling (Fan et al., 2010). To record disynaptic inhibition in CA1 pyramidal neurons, the intrapipette concentration of KCl was decrease to 4 mM.

Glass stimulating electrodes filled with extracellular saline were placed in the stratum radiatum. In control and test conditions, EPSPs were evoked at 0.1 Hz. The stimulus intensity (80–180 µs, 40–100 µA) was adjusted to evoke subthreshold EPSPs (~4–10 mV in pyramidal cells or interneurons; (Campanac et al., 2008; Daoudal et al., 2002)). In a subset of experiments, disynaptic IPSPs were evoked by stimulation of the Schaffer collaterals. These IPSPs were blocked by PTx (100 µM) (Lamsa et al., 2005), unmasking a large excitatory synaptic component followed by a hyperpolarization mediated by h-channels (Figure S1Figure S1; Gastrein et al., 2011). The ionotropic glutamate receptor antagonist, kynurenate (2 mM) also blocked evoked inhibition by 86.2% ± 2.5% (n = 6; Figure S1Figure S1), indicating that most of the evoked inhibition was disynaptic. LTP-IE was induced by high-frequency stimulation (HFS) consisting in 10 bursts delivered at 0.3 Hz each composed of 10 stimulations at 100 Hz.

Drugs were bath applied. PiTX, kynurenate and 4-aminopyridine (4-AP) were purchased from Sigma-Aldrich and DTx-I from Latoxan. (S)-3,5-dihydroxyphenylglycine(DHPG), (R,S)-2-chloro-5-hydroxyphenylglycine (CHPG), 2-methyl-6-phenylethynyl-pyriidine (MPEP) were obtained from Tocris.

The identity of the recorded neurons was confirmed by their firing pattern in response to depolarizing pulses of current and by the morphology of their axon. PV-BCs exhibited clustered and fast spiking firing patterns in response to depolarization, high spontaneous synaptic activity and low input resistance (120 ± 9 MΩ, n = 22). Compared to pyramidal cells, the half-width of their spike was narrow (0.64 ± 0.04 ms, n = 7) and their fast AHP was extremely deep (22 ± 1 mV, n = 7). The dendritic and axonal morphology of the recorded neurons was revealed by biocytin staining. Axons displayed characteristic basket-forming patterns. Biocytin (0.2%–0.4% Sigma) was added to the pipette solution and was revealed with avidin-biotin complex coupled to fluorescein, and examined using confocal microscopy (Leica TCS SP2).

Dynamic Clamp and Stimulation

In order to evaluate the EPSP-spike coupling in physiological conditions (Figure 1Figure 1E), families of AMPA-like EPSPs were simulated by a dynamic-clamp amplifier (SM1; Cambridge Conductance, Cambridge, UK) driven by PClamp 10-controlled digidata 1440A. The dynamic EPSC, EPSCdyn was defined as follows: EPSCdyn = g(Vm − Erev), where g is the synaptic conductance, Vm the membrane potential of the recorded neuron and Erev the reversal potential (0 mV). Conductance waveforms were generated with a double exponential function, $f(t) = a(1-exp(−t/τON))exp(−t/τOFF)$, with τON = 1 ms and τOFF = 10 ms.

The impedance amplitude profile (ZAP) method was used to characterize the electrical resonance of PV-BCs (Gastrein et al., 2011; Hutcheon and Yarom, 2000). Briefly, a sinusoidal current with constant amplitude and linearly increasing frequency (10–80 Hz for 3 s) was injected into the interneuron and the voltage response was recorded. The cell impedance as a function of frequency was given by the ratio of the fast-Fourier transform (FFT) of the voltage response to the magnitude of the FFT of the input current.

To assess the tonic firing properties of PV-BCs in natural conditions (Figure S5Figure S5), bursts of simulated EPSPs (mean frequency 40 Hz) were injected into the recorded neurons. The profile of each EPSC was determined by two exponentials (EPSC rise time: 1 ms, decay = 10 ms). The temporal pattern of the burst of EPSPs was randomly determined, but the selected pattern was presented at 10 s intervals with constant parameters throughout the whole experiment.

Data Acquisition and Analysis

Electrophysiological recordings were obtained using an Axopatch 2B amplifier and PClamp 9 or PClamp 10 (Axon Instruments, Molecular Devices). Data were analyzed with IGOR version 5 and 6 (WaveMetrics, Lake Oswego, OR) and Clampfit 10 (Axon Instruments, Molecular Devices). Input resistance and membrane time constant (τm) were calculated from voltage responses to small negative current pulses (typically −20 pA, 50 ms). To estimate τm the voltage responses were fitted with single exponentials. The spike threshold was measured as the voltage at which the first derivative of voltage (dV/dt) exceeded the threshold (20 mV/ms). Sparse and clustered spikes were distinguished on the bases of their threshold (see Figure S5Figure S5). Pooled data are presented as

either mean ± SEM or box plots and statistical analysis was performed in SigmaPlot 10 using the Mann-Whitney U test or the Wilcoxon test for paired data. XLSTAT (Addinsoft) was used for cluster analysis of the spike threshold versus instantaneous spike frequency data with the agglomerative hierarchical clustering method.

Immunostaining and Confocal Microscopy

After electrophysiological recordings, slices were allowed to rest for 1 hr in the recording chamber and then were transferred into 4% paraformaldehyde in phosphate buffer (PB) 0.1 M overnight at 4°C. After several washes in PB, slices were incubated for 1h in 5% normal donkey serum (Jackson ImmunoResearch Laboratories, West Grove, PA, USA) in PB containing 0.9% NaCl supplemented with 0.3% Triton X-100 (PBST) and incubated overnight in PBST containing a monoclonal mouse antibody against parvalbumin (1/500; clone PARV-19, Sigma-Aldrich, Saint Louis, MO, USA, reference P3088) and FITC-streptavidin (1/1000; Vector Laboratories, Burlingame, CA, USA). Slices were incubated for 3 hr in PBST containing donkey anti-mouse coupled to Cy5 (1/500; Jackson ImmunoResearch Laboratories Inc.) and FITC-streptavidin. Finally, they were mounted on slides and coverslipped in glycerol-PB 0.2 M (50:50) as mounting medium.

Immunostaining of Kv1.1 and Kv1.2 was performed on fixed hippocampal tissue. Briefly, P19–P20 rats were deeply anesthetized and perfused intracardially with paraformaldehyde (4%). The hippocampus was isolated, washed in PBS and transversal slices of 50 μm were sectioned with a vibratome (Leica VT-1000S). Triple labeling of parvalbumin (goat, 1/2000; PVG-214, Swant), Kv1.1 (extracellular, mouse, 1/50, NeuroMAB) or Kv1.2 (intracellular, mouse 1/50, NeuroMAB) and ankyrin G (rabbit, 1/500, A30). Secondary antibodies were raised in donkey and tagged with distinct fluorophores (anti-mouse Alexa 488; anti-goat Alexa 649 and anti-rabbit Alexa 594).

Confocal image acquisition was performed on a Leica TCS SP2 laser scanning microscope (Leica Microsystems, Heidelberg, Germany) using the 488 nm band of an Ar laser for excitation of Alexa-Fluor 488 (spectral detection: 492–544 nm), and the 633 nm band of an He-Ne laser for excitation of Cy5 (spectral detection 661–834 nm). Labeled neurons were scanned using a 20x oil lens (0.7 NA) from bottom to top (final voxel size was 0.73 μm in x, and y, and 1 μm in z). Reconstruction was obtained by maximum intensity projection of image stacks along the z axis (public domain NIH Image program, ImageJ, developed at the US National Institute of Health). Higher magnification images were obtained using a 40× oil lens (1.25 NA). Image editing was performed using Adobe Photoshop (Adobe Systems France).

Modeling

Computer simulations were performed with Neuron 7.2. The simplified morphology of a PV-BC included dendrite, soma, AIS, axon, and nerve terminal. The diameter, length, and number of subcompartment in each neuronal element are provided in Table S1Table S1. The membrane capacitance (Cm) was set to 1.2 μF/cm2 uniformly throughout all compartments. Axial resistance (Ri) was set to 100 Ωcm in the AIS and terminal, 200 Ωcm in the soma, dendrites, and axon. The leak conductance varied in the different compartments and was set to 0.15 mS/cm2 in the soma, 0.05 mS/cm2 in the dendrite, 0.15 mS/cm2 in the AIS, 0.02 mS/cm2 in the axon and 0.15 mS/cm2 in the terminal. The reversal potential for the leak conductance was –69 mV. All simulations were run with 10 μs time steps and the nominal temperature of simulations was 25°C. The voltage dependence of

activation and inactivation of a Hodgkin-Huxley based transient Na+ and delayed rectifier K+ (KDR) channel model was based on the study of Wang & Buzsaki (Wang and Buzsáki, 1996). The equilibrium potential for Na+ and K+ was set to +60 mV and −85 mV, respectively. The densities of Na+ channels and KDR channels in each compartment are provided in Table S1Table S1. The model also included a D-type, slowly inactivating conductance (Kv1). The biophysical parameters of the D-type conductance were taken from a previous study (Golomb et al., 2007). Three repartitions were tested. In the first, D-type channels were located in the AIS (0.65 S/cm2) and in the axon (0.25 S/cm2) but not in the soma (0 S/cm2). In the second repartition, D-type channels were principally located in the soma (0.085 S/cm2 and only 0.01 S/cm2 in the axon) but not in the AIS (0 S/cm2). Finally, in the third repartition, the density of D-type channel was 0 in the soma, AIS and axon. In all cases, the action potential was initiated in the AIS and back-propagated in the dendrites as observed experimentally (data not shown; Hu et al., 2010 ; Nörenberg et al., 2010).

References

Alle, H., Jonas, P., and Geiger, J.R. (2001). PTP and LTP at a hippocampal mossy fiber-interneuron synapse. Proc Natl Acad Sci U S A *98*, 14708-14713.

Campanac, E., Daoudal, G., Ankri, N., and Debanne, D. (2008). Downregulation of dendritic I(h) in CA1 pyramidal neurons after LTP. J Neurosci *28*, 8635-8643.

Campanac, E., and Debanne, D. (2008). Spike timing-dependent plasticity: a learning rule for dendritic integration in rat CA1 pyramidal neurons. J Physiol *586*, 779-793.

Cudmore, R.H., Fronzaroli-Molinieres, L., Giraud, P., and Debanne, D. (2010). Spike-time precision and network synchrony are controlled by the homeostatic regulation of the D-type potassium current. J Neurosci *30*, 12885-12895.

Daoudal, G., Hanada, Y., and Debanne, D. (2002). Bidirectional plasticity of excitatory postsynaptic potential (EPSP)-spike coupling in CA1 hippocampal pyramidal neurons. Proc Natl Acad Sci U S A *99*, 14512-14517.

Debanne, D., and Poo, M.M. (2010). Spike-timing dependent plasticity beyond synapse - pre- and post-synaptic plasticity of intrinsic neuronal excitability. Front Synaptic Neurosci *2*, 21.

Desai, N.S. (2003). Homeostatic plasticity in the CNS: synaptic and intrinsic forms. J Physiol Paris *97*, 391-402.

Fan, W., Ster, J., and Gerber, U. (2010). Activation conditions for the induction of metabotropic glutamate receptor-dependent long-term depression in hippocampal CA1 pyramidal cells. J Neurosci *30*, 1471-1475.

Freund, T.F., and Katona, I. (2007). Perisomatic inhibition. Neuron *56*, 33-42.

Frick, A., Magee, J., and Johnston, D. (2004). LTP is accompanied by an enhanced local excitability of pyramidal neuron dendrites. Nat Neurosci *7*, 126-135.

Froemke, R.C., Merzenich, M.M., and Schreiner, C.E. (2007). A synaptic memory trace for cortical receptive field plasticity. Nature *450*, 425-429.

Gastrein, P., Campanac, E., Gasselin, C., Cudmore, R.H., Bialowas, A., Carlier, E., Fronzaroli-Molinieres, L., Ankri, N., and Debanne, D. (2011). The role of hyperpolarization-activated cationic current in spike-time precision and intrinsic resonance in cortical neurons in vitro. J Physiol *589*, 3753-3773.

Glickfeld, L.L., and Scanziani, M. (2006). Distinct timing in the activity of cannabinoid-sensitive and cannabinoid-insensitive basket cells. Nat Neurosci *9*, 807-815.

Goldberg, E.M., Clark, B.D., Zagha, E., Nahmani, M., Erisir, A., and Rudy, B. (2008). K+ channels at the axon initial segment dampen near-threshold excitability of neocortical fast-spiking GABAergic interneurons. Neuron *58*, 387-400.

Golomb, D., Donner, K., Shacham, L., Shlosberg, D., Amitai, Y., and Hansel, D. (2007). Mechanisms of firing patterns in fast-spiking cortical interneurons. PLoS Comput Biol *3*, e156.

Gulyas, A.I., Szabo, G.G., Ulbert, I., Holderith, N., Monyer, H., Erdelyi, F., Szabo, G., Freund, T.F., and Hajos, N. (2010). Parvalbumin-containing fast-spiking basket cells generate the field potential oscillations induced by cholinergic receptor activation in the hippocampus. J Neurosci *30*, 15134-15145.

Higgs, M.H., and Spain, W.J. (2011). Kv1 channels control spike threshold dynamics and spike timing in cortical pyramidal neurones. J Physiol *589*, 5125-5142.

Hu, H., Martina, M., and Jonas, P. (2010). Dendritic mechanisms underlying rapid synaptic activation of fast-spiking hippocampal interneurons. Science *327*, 52-58.

Hutcheon, B., and Yarom, Y. (2000). Resonance, oscillation and the intrinsic frequency preferences of neurons. Trends Neurosci *23*, 216-222.

Isaacson, J.S., and Scanziani, M. (2011). How inhibition shapes cortical activity. Neuron *72*, 231-243.

Klann, E., and Dever, T.E. (2004). Biochemical mechanisms for translational regulation in synaptic plasticity. Nat Rev Neurosci *5*, 931-942.

Klausberger, T., and Somogyi, P. (2008). Neuronal diversity and temporal dynamics: the unity of hippocampal circuit operations. Science *321*, 53-57.

Kullmann, D.M., and Lamsa, K.P. (2007). Long-term synaptic plasticity in hippocampal interneurons. Nat Rev Neurosci *8*, 687-699.

Kullmann, D.M., Moreau, A.W., Bakiri, Y., and Nicholson, E. (2012). Plasticity of inhibition. Neuron *75*, 951-962.

Lamsa, K., Heeroma, J.H., and Kullmann, D.M. (2005). Hebbian LTP in feed-forward inhibitory interneurons and the temporal fidelity of input discrimination. Nat Neurosci *8*, 916-924.

Lamsa, K.P., Heeroma, J.H., Somogyi, P., Rusakov, D.A., and Kullmann, D.M. (2007). Anti-Hebbian long-term potentiation in the hippocampal feedback inhibitory circuit. Science *315*, 1262-1266.

Lewis, D.A., Curley, A.A., Glausier, J.R., and Volk, D.W. (2012). Cortical parvalbumin interneurons and cognitive dysfunction in schizophrenia. Trends Neurosci *35*, 57-67.

Li, K.X., Lu, Y.M., Xu, Z.H., Zhang, J., Zhu, J.M., Zhang, J.M., Cao, S.X., Chen, X.J., Chen, Z., Luo, J.H., *et al.* (2012). Neuregulin 1 regulates excitability of fast-spiking neurons through Kv1.1 and acts in epilepsy. Nat Neurosci *15*, 267-273.

Maccaferri, G., Toth, K., and McBain, C.J. (1998). Target-specific expression of presynaptic mossy fiber plasticity. Science *279*, 1368-1370.

Miles, R., and Poncer, J.C. (1993). Metabotropic glutamate receptors mediate a post-tetanic excitation of guinea-pig hippocampal inhibitory neurones. J Physiol *463*, 461-473.

Miller, M.N., Okaty, B.W., Kato, S., and Nelson, S.B. (2011). Activity-dependent changes in the firing properties of neocortical fast-spiking interneurons in the absence of large changes in gene expression. Dev Neurobiol *71*, 62-70.

Norenberg, A., Hu, H., Vida, I., Bartos, M., and Jonas, P. (2010). Distinct nonuniform cable properties optimize rapid and efficient activation of fast-spiking GABAergic interneurons. Proc Natl Acad Sci U S A *107*, 894-899.

Nusser, Z. (2009). Variability in the subcellular distribution of ion channels increases neuronal diversity. Trends Neurosci *32*, 267-274.

Pelletier, J.G., and Lacaille, J.C. (2008). Long-term synaptic plasticity in hippocampal feedback inhibitory networks. Prog Brain Res *169*, 241-250.

Raab-Graham, K.F., Haddick, P.C., Jan, Y.N., and Jan, L.Y. (2006). Activity- and mTOR-dependent suppression of Kv1.1 channel mRNA translation in dendrites. Science *314*, 144-148.

Ross, S.T., and Soltesz, I. (2001). Long-term plasticity in interneurons of the dentate gyrus. Proc Natl Acad Sci U S A *98*, 8874-8879.

Sourdet, V., Russier, M., Daoudal, G., Ankri, N., and Debanne, D. (2003). Long-term enhancement of neuronal excitability and temporal fidelity mediated by metabotropic glutamate receptor subtype 5. J Neurosci *23*, 10238-10248.

Sun, Q.Q. (2009). Experience-dependent intrinsic plasticity in interneurons of barrel cortex layer IV. J Neurophysiol *102*, 2955-2973.

Szabo, G.G., Holderith, N., Gulyas, A.I., Freund, T.F., and Hajos, N. (2010). Distinct synaptic properties of perisomatic inhibitory cell types and their different modulation by cholinergic receptor activation in the CA3 region of the mouse hippocampus. Eur J Neurosci *31*, 2234-2246.

Wang, X.J., and Buzsaki, G. (1996). Gamma oscillation by synaptic inhibition in a hippocampal interneuronal network model. J Neurosci *16*, 6402-6413.

Wang, Z., Xu, N.L., Wu, C.P., Duan, S., and Poo, M.M. (2003). Bidirectional changes in spatial dendritic integration accompanying long-term synaptic modifications. Neuron *37*, 463-472.

Whittington, M.A., Traub, R.D., and Jefferys, J.G. (1995). Synchronized oscillations in interneuron networks driven by metabotropic glutamate receptor activation. Nature *373*, 612-615.

Yazaki-Sugiyama, Y., Kang, S., Cateau, H., Fukai, T., and Hensch, T.K. (2009). Bidirectional plasticity in fast-spiking GABA circuits by visual experience. Nature *462*, 218-221.

Yu, F.H., Mantegazza, M., Westenbroek, R.E., Robbins, C.A., Kalume, F., Burton, K.A., Spain, W.J., McKnight, G.S., Scheuer, T., and Catterall, W.A. (2006). Reduced sodium current in GABAergic interneurons in a mouse model of severe myoclonic epilepsy in infancy. Nat Neurosci *9*, 1142-1149.

Zhang, W., and Linden, D.J. (2003). The other side of the engram: experience-driven changes in neuronal intrinsic excitability. Nat Rev Neurosci *4*, 885-900.
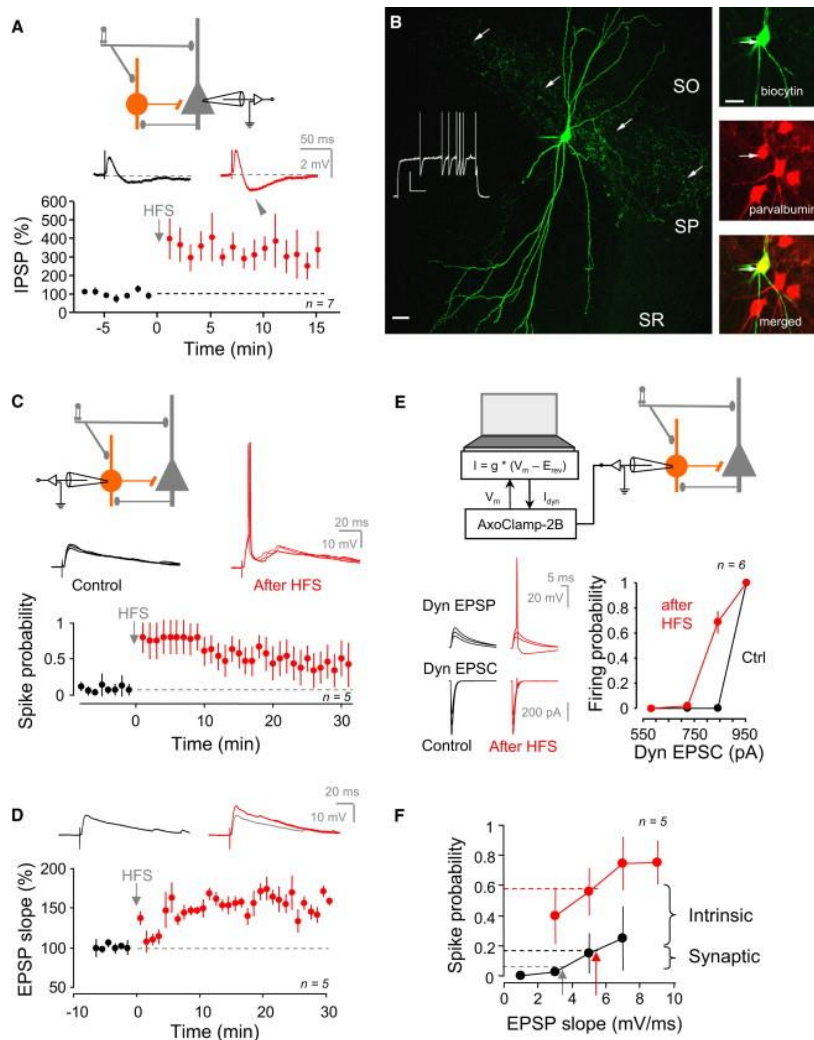
Figure 1

Excitatory-Inhibitory Balance Is Mediated by Both Synaptic and Intrinsic Changes

(A) Top, recording and stimulation configuration. Bottom, a long-lasting increase in disynaptic inhibition recorded in CA1 pyramidal neurons is induced by high frequency stimulation (HFS) of the Schaffer collaterals.

(B) Morphological identification of parvalbumin-positive basket cells (PV-BC). Left, confocal image of a fast-spiking (white trace) interneuron filled with biocytin. Note the vertically oriented dendritic tree in the stratum radiatum (SR) and stratum oriens (SO) and the axon arborization concentrated in the stratum pyramidale (SP, white arrows). Insets, the soma (arrows) and some primary dendrites are immunoreactive for parvalbumin. Scale bars 40 μm and 25 μm (inset).

(C) Firing probability of PV-BC evoked by the EPSP after HFS.

(D) Long-term potentiation of excitatory synaptic transmission in PV-BCs.

(E) Persistent increase in intrinsic neuronal excitability induced in PV-BCs by HFS. Left, recording configuration using the dynamic-clamp system. Families of simulated dynamic EPSPs are generated before and after HFS. Note the increase in spiking activity after HFS. Right, input-output curves expressing the firing probability as a function of the dynamic EPSC amplitude.

(F) EPSP-spike curves established with the five cells illustrated in (C) and (D). Black points, before HFS. Red points, after HFS. The vertical gray arrow indicates the mean EPSP-slope before HFS and the red arrow symbolizes the mean EPSP-slope after HFS. Dashed gray line, firing probability before HFS; dashed red line, firing probability after HFS; dashed black line, firing probability obtained by a pure synaptic modification.

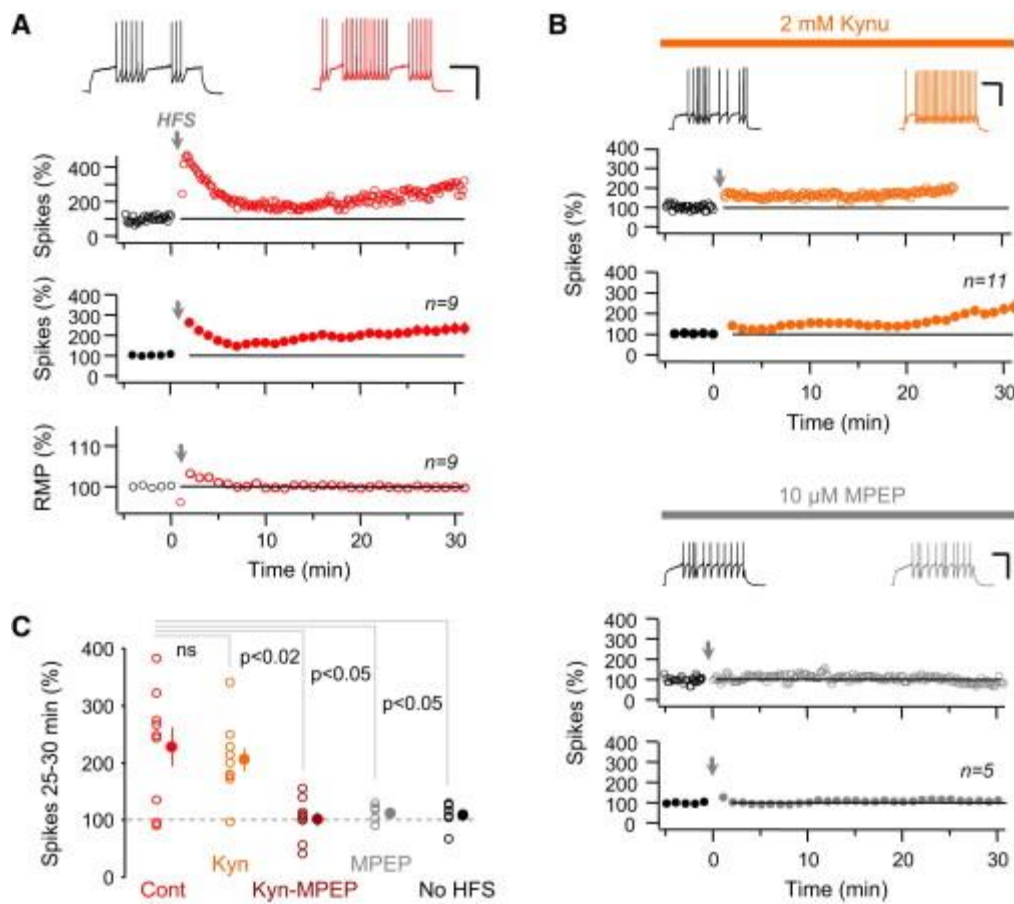Error bars indicate SEM. See also Figure S1.

Figure 2

Induction Mechanisms of Synaptically Generated LTP-IE$_{PV-BC}$

(A) Time course of LTP-IE$_{PV-BC}$ in a representative neuron (top) and 9 cells (middle). Note the transient component and the plateau of potentiation. Bottom, time course of the resting membrane potential (RMP).

(B) Pharmacological dissection of LTP-IE$_{PV-BC}$. Representative example and group data of the effects of HFS in the presence of kynurenate (top) or MPEP (bottom). Scale bars: 200 ms and 40 mV.

(C) Group data of LTP-IE$_{PV-BC}$ measured 25–30 min after HFS in the different conditions (Mann-Whitney U test for statistics).
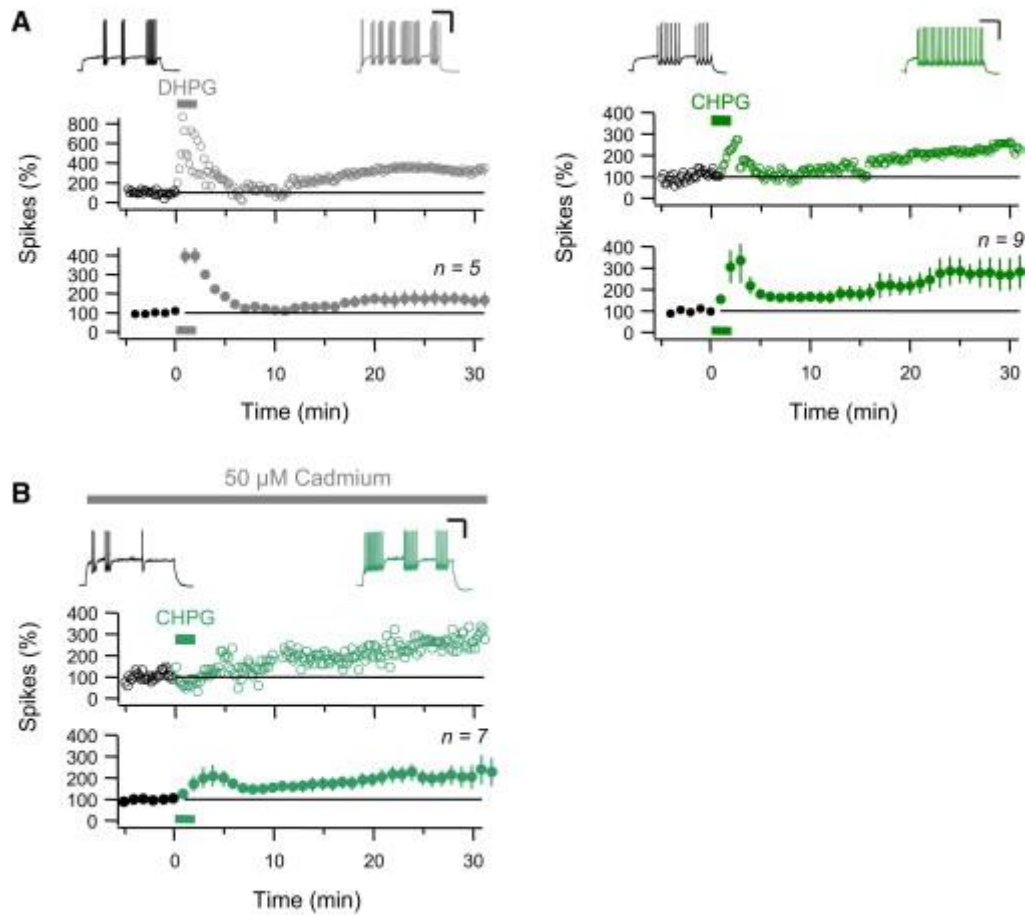
Error bars indicate SEM. See also Figure S2.

Figure 3

Pharmacological Induction of LTP-IE in PV-BCs

(A) Left, LTP-IE$_{PV-BC}$ was induced by brief application of the mGluR1-5 agonist DHPG (20 μM, 2 min). Upper graph, representative example. Middle graph, pooled data. Right, induction of LTP-IE$_{PV-BC}$ by brief application of the mGluR5 agonist CHPG (200–500 μM, 2 min). Note the presence in both cases of two components. The transient component is due to a depolarization of the neuron but the sustained component is independent of any change in membrane potential.

(B) Induction of LTP-IE$_{PV-BC}$ by CHPG (500 μM) in the presence of cadmium (50 μM).
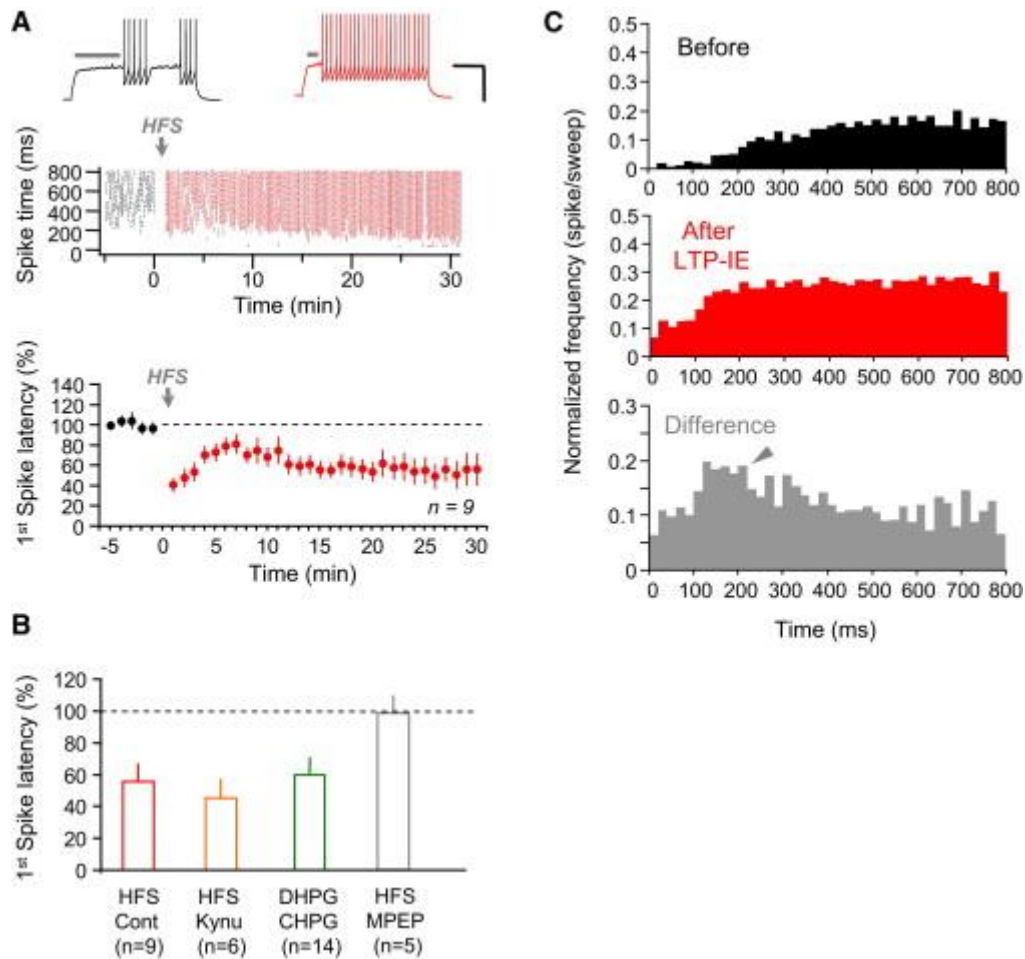
Error bars indicate SEM.

Figure 4

Modulation of the Temporal Profile of the Discharge after LTP-IE$_{PV-BC}$

(A) Reduced first spike latency in PV-BCs after HFS. Top, scatter plot of spike timing over time in a representative example. Bottom, time course of the first spike latency in nine interneurons.

(B) Pooled data.

(C) Analysis of the temporal discharge of PV-BC before (black histogram) and after (red histogram) HFS. Each histogram (bin, 20 ms) corresponds to the average of nine cells. The gray histogram represents the difference (red-black). Note the phasic increase peaking at ~150 ms (arrow head) on the tonic increase in firing.
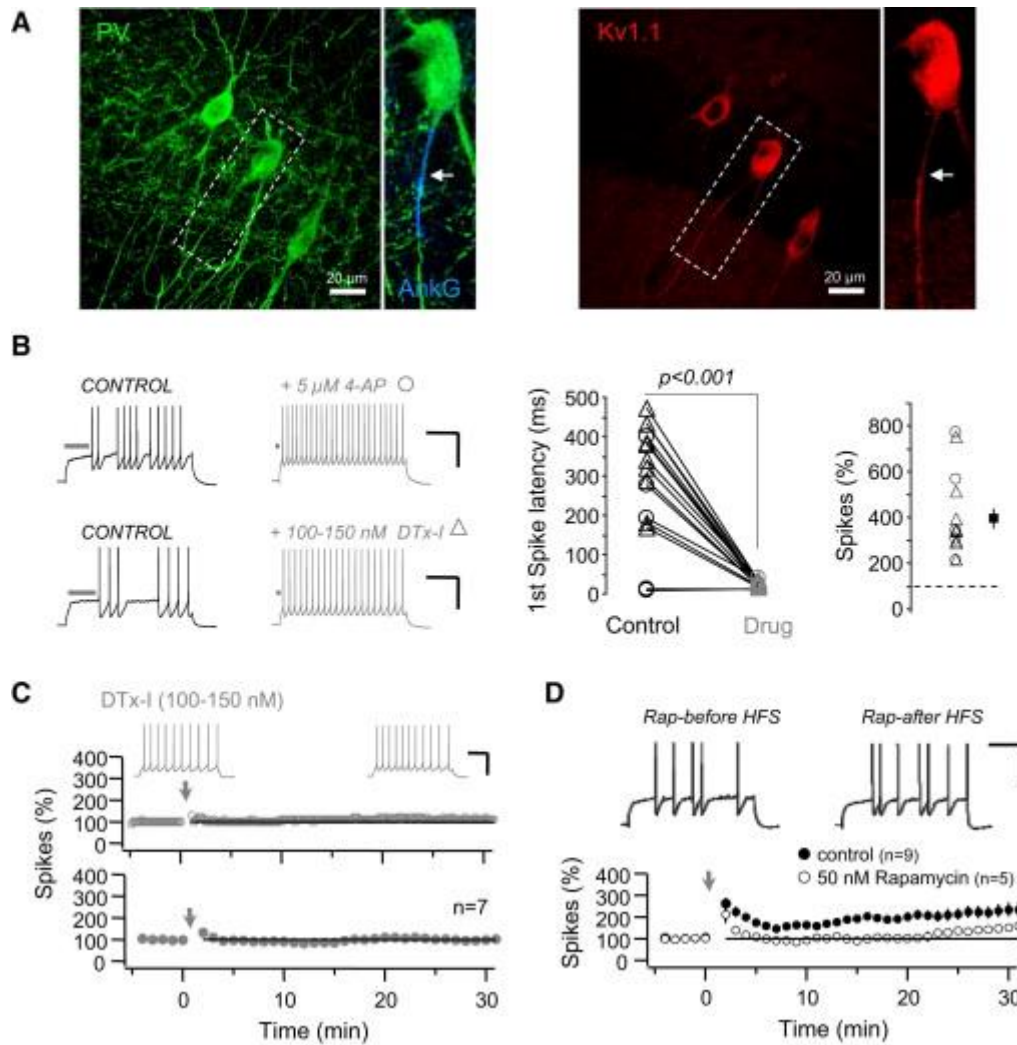
Error bars indicate SEM.

Figure 5

Expression Mechanisms of LTP-IE$_{PV-BC}$: Role of Kv1 Channels

(A) Immunolabeling of parvalbumin (PV, left) and Kv1.1 subunit (right) in the stratum pyramidale of the CA1 region. Inset, identification of the axon initial segment of PV-positive neurons with ankyrin G labeling (AnkG, white arrow). Note the strong labeling of Kv1.1 channels in the cell body and in the axon of PV-positive neurons (see inset, white arrow).

(B) Effects of Kv channel blockers on the first spike latency and spike number. Left, representative examples. Right, group data showing the reduced latency of the first spike (Wilcoxon test for statistics) and the enhanced excitability.

(C) Occlusion of LTP-IE$_{PV-BC}$ by the Kv1 channel blocker DTx-I.

(D) Occlusion of LTP-IE$_{PV-BC}$ by the inhibitor of mTOR, rapamycin. Scale bars: 200 ms and 40 mV.

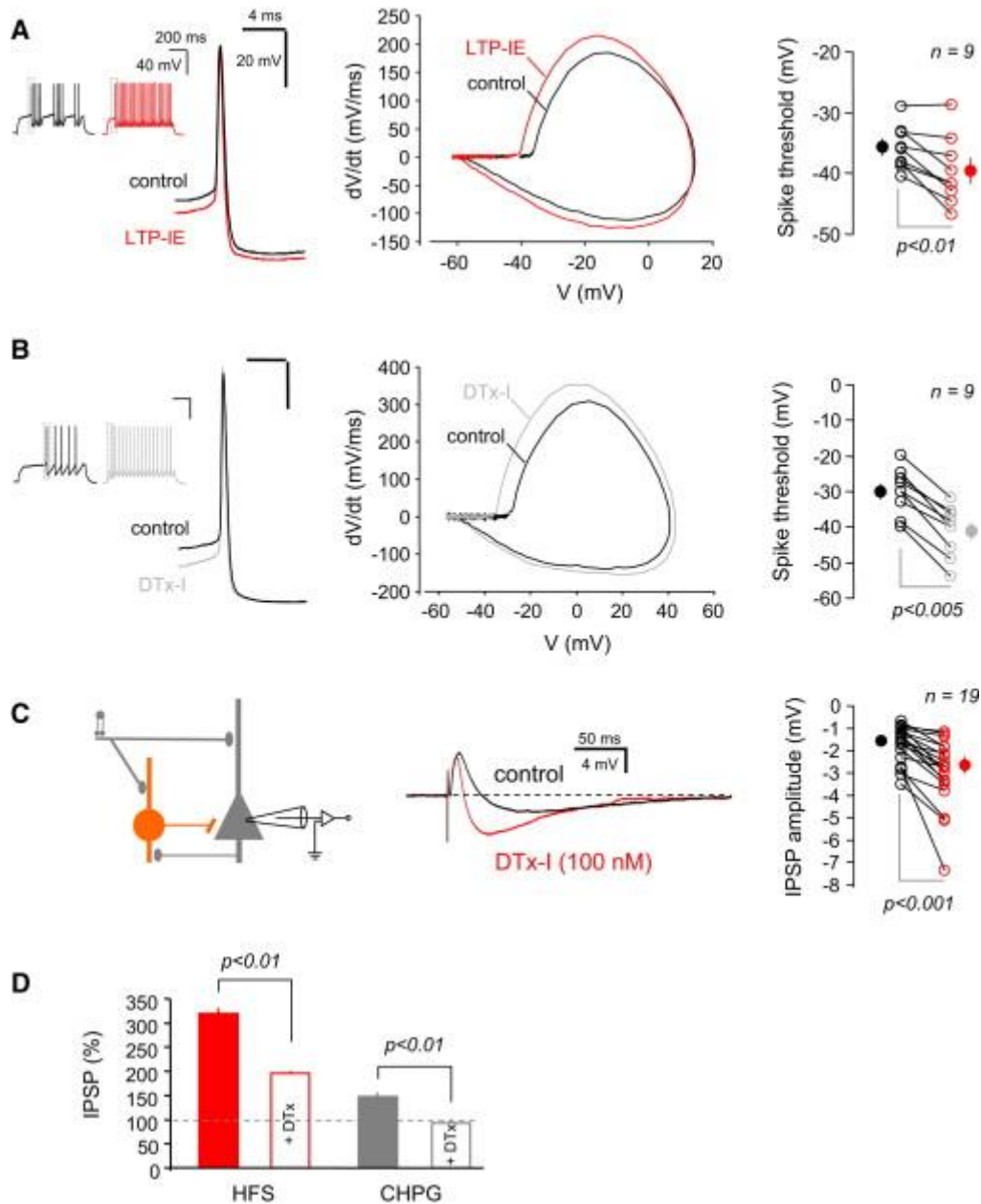Error bars indicate SEM. See also Figure S3.

Figure 6

Changes in Spike Threshold and Contribution of Kv1 Channels to the Dynamics of Feed-Forward Inhibition

(A) Hyperpolarization of the spike threshold induced by HFS. Left, comparison of the first spike threshold in a representative example before and after induction of LTP-IE$_{PV-BC}$. Middle, phase plot of the action potential before and after induction of LTP-IE$_{PV-BC}$. Right, group data.

(B) Hyperpolarization of the spike threshold induced by DTx-I in PV-BCs.

(C) Increase in disynaptic inhibition induced by the pharmacological blockade of Kv1.1 with DTx-I. Wilcoxon test was used for statistics (A–C).

(D) DTx-I reduced or occluded facilitation of disynaptic inhibition induced by HFS or CHPG. Note that the facilitation of feed-forward inhibition induced by HFS amounted to 39% of the control, suggesting that the synaptic contribution to this facilitation is minor. Mann-Whitney test was used for statistics. Error bars indicate SEM. See also Figure S4.
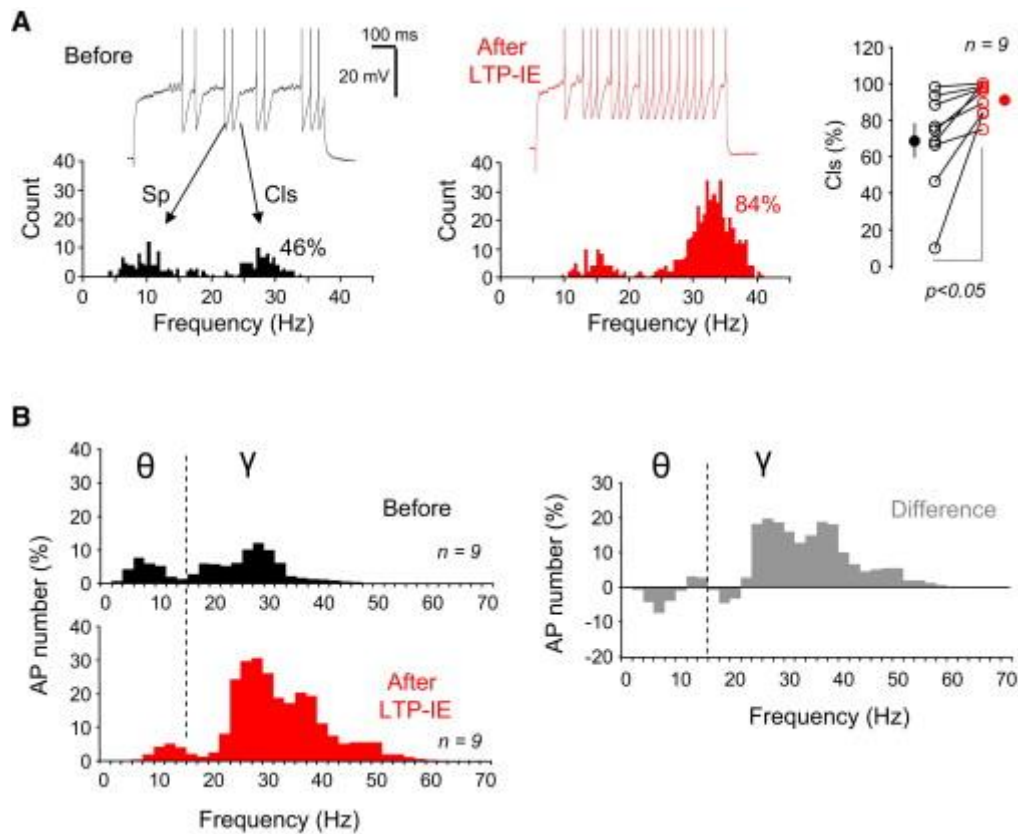
Figure 7
Increase in Clustered-Spiking Activity in the Gamma-Frequency Range after Induction of LTP-IE$_{PV-BC}$
(A) Example of PV-BC showing an increase in the proportion of spikes in clusters (Cls) measured 15–30 min after HFS (left). Right, pooled data. The Wilcoxon test was used for statistics.
(B) Group data. Black histogram, mean of normalized spiking histogram for the 9 cells before HFS. The dashed line symbolizes the limit between θ and γ frequency. Red histogram, after HFS. The histograms for each neuron were normalized to each control. Grey histogram, difference bin by bin between the two previous histograms. Note the increased spiking activity in the γ range.
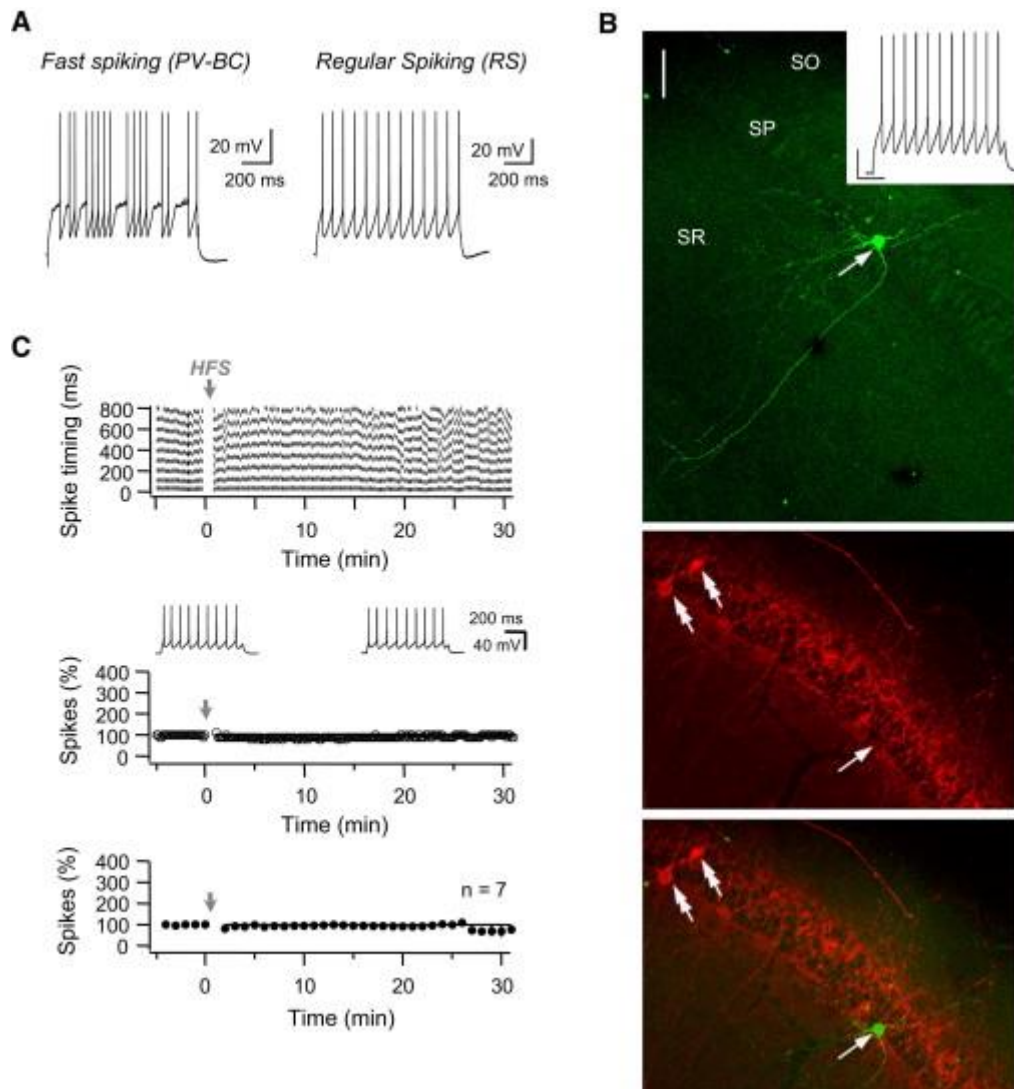Error bars indicate SEM. See also Figure S5.

Figure 8

Regular Spiking PV-Negative Interneurons Do Not Express LTP-IE

(A) Comparison of discharge profiles of fast spike PV-BC (left) and regular spiking (RS) interneurons (right).

(B) Morphological identification of regular spiking interneurons. Top biocytin labeling (green) and discharge profile of the recorded interneuron. Red, PV immunostaining. Note the lack of PV in the recorded cell (single arrow), but the staining of two neighboring neurons (double arrows). Scale bar: 73 μm.

(C) Lack of LTP-IE in regular spiking interneurons. Top, raster plot of the spikes showing the regularity of the discharge. Middle, example of a RS interneuron displaying no LTP-IE. Bottom, group data. Vertical arrows indicate HFS.

Error bars indicate SEM. See also Figure S6.